

ION TEMPERATURES IN THE LOW SOLAR CORONA: POLAR CORONAL HOLES AT SOLAR MINIMUM

E. LANDI

Artep, Inc. at Naval Research Laboratory, 4555 Overlook Ave. S.W., 20375-5320, Washington DC

S. R. CRANMER

Harvard-Smithsonian Center for Astrophysics, 60 Garden Street, Cambridge, MA 02138

Draft version November 10, 2018

ABSTRACT

In the present work we use a deep-exposure spectrum taken by the SUMER spectrometer in a polar coronal hole in 1996 to measure the ion temperatures of a large number of ions at many different heights above the limb between 0.03 and 0.17 solar radii. We find that the measured ion temperatures are almost always larger than the electron temperatures and exhibit a non-monotonic dependence on the charge-to-mass ratio. We use these measurements to provide empirical constraints to a theoretical model of ion heating and acceleration based on gradually replenished ion-cyclotron waves. We compare the wave power required to heat the ions to the observed levels to a prediction based on a model of anisotropic magnetohydrodynamic turbulence. We find that the empirical heating model and the turbulent cascade model agree with one another, and explain the measured ion temperatures, for charge-to-mass ratios smaller than about 0.25. However, ions with charge-to-mass ratios exceeding 0.25 disagree with the model; the wave power they require to be heated to the measured ion temperatures shows an increase with charge-to-mass ratio (i.e., with increasing frequency) that cannot be explained by a traditional cascade model. We discuss possible additional processes that might be responsible for the inferred surplus of wave power.

Subject headings: line: profiles — Sun: corona — Sun: UV radiation — techniques: spectroscopic — turbulence — waves

1. INTRODUCTION

In order to understand the physical processes that heat the solar corona and accelerate the solar wind, theories must be able to predict measurements of the plasma parameters in the regions that are being heated and accelerated. In the low-density, open-field regions that correspond to polar coronal holes on the Sun, the plasma is expected to become collisionless very near the solar surface, and thus the individual particle species (e.g., protons, electrons, and heavy ions) may exhibit diverging properties. These differences are key probes of the microscopic kinetic physics that drives the heating and acceleration. The Solar Ultraviolet Measurements of Emitted Radiation (SUMER) spectrometer aboard the *Solar and Heliospheric Observatory (SOHO)* has measured these properties for more than a decade (see, e.g., Wilhelm et al. 1995, 1997).

Inspired by both the SUMER observations presented below and other remote-sensing and in situ measurements, we focus on the damping of ion cyclotron resonant Alfvén waves as a natural means of preferentially heating and accelerating coronal ions. Efficient kinetic interactions between ion cyclotron waves and particle velocity distributions in the solar wind have been studied for several decades (e.g., Abraham-Shrauner & Feldman 1977; Hollweg & Turner 1978; Marsch et al. 1982; Hollweg 1986; Tu & Marsch 1997; Cranmer et al. 1999a; Hollweg & Isenberg 2002; Cranmer 2002; Kohl et al. 2006). Despite much intense theoretical work, the origin of the high-frequency (10^2 – 10^4 Hz) cyclotron waves in the solar corona is not yet known. Most ideas for the generation of these waves fall into two classes: (1) excitation at the base of the corona, and (2) gradual growth or replenishment of cyclotron waves throughout the corona and solar wind. The first idea has been proposed to occur from impulsive processes

taking place in magnetically complex regions (e.g., reconnection in microflares; see Axford & McKenzie 1992; Ruzmaikin & Berger 1998). The second scenario has been proposed to occur mainly from magnetohydrodynamic (MHD) turbulent cascade (Isenberg & Hollweg 1983; Cranmer & van Ballegoijen 2003; Chandran 2005), but other processes such as kinetic microinstabilities have also been suggested. Indirect support for the second idea of “gradual replenishment” has come from empirical studies of radio scintillations (Hollweg 2000) and theoretical models of the charge and mass dependence of the wave damping (Cranmer 2000, 2001). In our paper, we will base our model on the gradual replenishment scenario.

One of the main predictions of ion-cyclotron models is preferential heating and acceleration of ions in the solar wind, with the effect of waves on ions being dependent on the Z_i/A_i ratio, where Z_i is the ion’s charge and A_i its atomic mass (with both usually specified in proton units). One of the observables that can best constrain theoretical models of ion-cyclotron waves is the behavior of the *ion temperature* (i.e., the magnitude of ion random motions on microscopic scales). These models are also dependent on the overall amplitude of MHD waves in the corona, which can also be constrained empirically by the so-called *non-thermal* component of emission line profiles.

Measuring ion temperatures and non-thermal velocities is however a very difficult task, as these are two separate physical quantities that have to be determined from one single observable, the line width. Thus, some assumptions have to be made. However, these limit the accuracy of the measurements. In the past, most assumptions were taken on the value of T_i , since the quantity of interest was the non-thermal velocity v_{nth} . The most common assumptions were $T_i = T_e$, or $T_i = T_M$, where T_M is the temperature of formation of the

line, usually taken as the temperature of maximum abundance of the ion emitting the line. A more elaborate set of assumptions were adopted by Seely et al. (1997), who assumed that ions formed in the same temperature range have the same T_i ; this allowed them to determine both T_i and v_{nth} from SUMER/SOHO observations. Tu et al. (1998), on the contrary, assumed that v_{nth} is the same for all ions. This allowed them to set an upper limit to v_{nth} , and conservatively assumed $v_{\text{nth}} = 0$ as a lower limit. From these limits, the range of possible T_i values could be determined. In doing this, Tu et al. (1998) limited the number of assumptions to the minimum and chose not to determine v_{nth} , so that they could set rather precise limits to T_i of the ions in their dataset. Dolla & Solomon (2008) went a step further by making assumptions not on the values of T_i or v_{nth} , but on the physical process that affects them. They assumed that: (1) non-thermal velocities are due to undamped Alfvén waves, and (2) that Mg x was not heated by them so that its T_i was constant and could be used to measure v_{nth} .

The aim of the present work is twofold. First, we will extend the analysis done by Tu et al. (1998) by applying their method to spectra emitted by coronal hole plasmas at the north pole, that include many more lines from many more ions than considered by them. We will repeat the T_i measurements for as many heights above the solar limb as made possible by the signal-to-noise ratio and instrument scattered light. This has been achieved by using deep-exposure SUMER spectra encompassing the entire wavelength range (500–1500 Å) included by detector B on SUMER.

Second, we will use the measured ion temperature values as constraints for semi-empirical theoretical models of ion heating and acceleration based on the damping of ion cyclotron resonant Alfvén waves. We will develop a model that is mainly intended to be illustrative of the proper ranges of plasma parameters that are consistent with the observations in the low corona, but not yet self-consistent enough to be considered a definitive or unique explanation of the SUMER data set.¹

The first part of the paper deals with the ion temperature measurements. Section 2 introduces the method of analysis and Section 3 describes the observations studied in the present work. Our measurements are reported in Section 4. The second part of the paper describes the comparison with the theoretical model. In Section 5 the separation of line widths into thermal and non-thermal parts is discussed in more detail. The physical processes assumed in the semi-empirical models are given in Section 6, and a comparison with a purely theoretical model of MHD turbulence is made in Section 7. The model results are shown and described in Section 8. Section 9 summarizes the present work.

2. METHOD OF ANALYSIS

In this work, we have applied the analysis method described by Tu et al. (1998), that we briefly summarize here. The measured full width half maximum (FWHM) $d\lambda$ of a spectral line can be related to the dynamical status of the emitting ion through the equation

$$d\lambda = \frac{\lambda_0}{c} \sqrt{4 \ln 2 \left(\frac{2k_B T_i}{M_i} + v_{\text{nth}}^2 \right)} \quad (1)$$

¹ Specifically, these models do *not* try to validate or disprove the assumption that the ion cyclotron waves are created by an anisotropic turbulent cascade; they only try to work out the implications of such an assumption.

where $d\lambda$ is the FWHM of the line after the instrumental broadening has been removed, T_i and $M_i = m_p A_i$ (m_p is the proton mass) are the ion’s temperature and mass, k_B is Boltzmann’s constant, c is the speed of light, λ_0 is the rest wavelength of the line, and v_{nth} is the ion’s non-thermal velocity. From equation (1), the ion temperature given by each line can not be larger than the value obtained when $v_{\text{nth}} = 0$:

$$T_i \leq T_{\text{max},i} \\ T_{\text{max},i} = \frac{m_p c^2}{8k_B \ln 2} A_i \left(\frac{d\lambda}{\lambda_0} \right)_i^2 = 1.96 \times 10^{12} A_i \left(\frac{d\lambda}{\lambda_0} \right)_i^2 \text{ K} \quad (2)$$

where A_i is the atomic mass. In the same way, the non-thermal velocity can not be larger than the value obtained when $T_i = 0$:

$$v_{\text{nth}} \leq v_{\text{max},i} \\ v_{\text{max},i} = \sqrt{\frac{c^2}{4 \ln 2} \left(\frac{d\lambda}{\lambda_0} \right)_i^2} = 1.80 \times 10^{10} \left(\frac{d\lambda}{\lambda_0} \right)_i \text{ cm s}^{-1}. \quad (3)$$

In order to determine a lower limit to T_i , it is necessary to make an assumption on v_{nth} . The method devised by Tu et al. (1998) allows us to determine the minimum T_i values compatible with a set of measured FWHM values by assuming that v_{nth} is the same for all ions. If we define v_{min} as the smallest among the $v_{\text{max},i}$ values obtained from a set of lines, the ion temperature of each ion must be larger than the value obtained when $v_{\text{nth}} = v_{\text{min}}$. If we indicate with j the line for which $v_{\text{nth}} = v_{\text{min}}$, the range of ion temperatures compatible with the FWHM measured with line i is given by

$$\frac{m_p c^2}{8k_B \ln 2} A_i \left[\left(\frac{d\lambda}{\lambda_0} \right)_i^2 - \left(\frac{d\lambda}{\lambda_0} \right)_j^2 \right] \leq T_i \leq \frac{m_p c^2}{8k_B \ln 2} A_i \left(\frac{d\lambda}{\lambda_0} \right)_i^2 \quad (4)$$

Note that the lower limit of T_i for line j is zero. The interval defined by equation (4) is not to be considered the “error bar” due to experimental uncertainties in the measurement of the line’s FWHM; it indicates the range of equally possible T_i values allowed by the observed FWHM value. Uncertainties in the measured $d\lambda$ are propagated to the limit values of T_i in equation (4), and widen the range of possible ion temperatures. This method of analysis has the advantage of reducing the assumptions on T_i and v_{nth} to the very minimum. However, it only provides us with an upper limit to v_{nth} .

3. OBSERVATIONS AND DATA REDUCTION

3.1. Observations

Observations were taken on 1996 November 3, and consist of a full spectral scan encompassing the entire SUMER wavelength range carried out over a polar coronal hole. The center of the slit field of view was (0′′, 1149′′), so that coronal hole plasma was observed at heliocentric distances between 1.03 solar radii (R_\odot) and 1.33 R_\odot . The instrument configuration allows the recording of the solar spectrum in $\simeq 43$ Å-wide subsections of the 500–1600 Å spectral range; in the present observation the full SUMER range was observed in 61 subsections, each shifted from the previous one by $\simeq 13$ Å. This ensured that all lines were observed on the more sensitive KBr-coated portion of the detector at least once. Each spectral subsection was observed with SUMER detector B with 1200 s exposure time, so that the final effective wavelength range of the dataset we studied is 500–1500 Å. An image of the SUMER field of view superimposed to EIT images is shown in Figure 1.

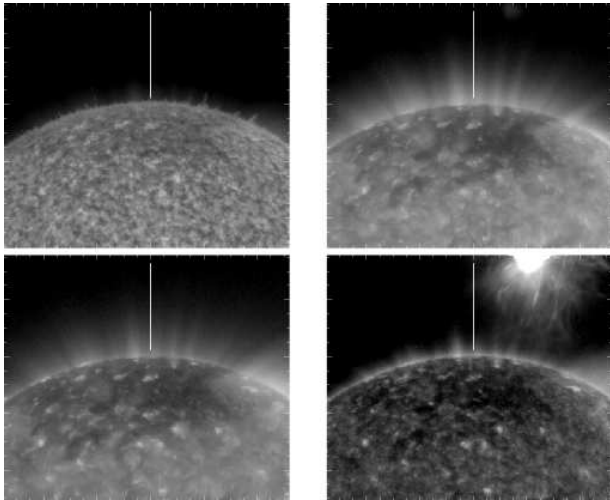


FIG. 1.— Field of view of the SUMER slit, superimposed to EIT images in all four filters: *Top left*: He II (5×10^4 K); *Top right*: Fe IX-X (6.3×10^5 K); *Bottom left*: Fe XII (1.4×10^6 K); *Bottom right*: Fe XV (2.2×10^6 K). The EIT images were taken on the same day as SUMER (3 November 1996) between 1 UT and 2 UT.

TABLE 1
LINES USED FOR THE PRESENT STUDY. R_{\max} (IN UNITS OF SOLAR RADII FROM DISK CENTER) INDICATES THE MAXIMUM DISTANCE BEYOND WHICH THE LINE COULD NOT BE USED DUE TO SCATTERED LIGHT CONTAMINATION.

Ion	Wvl. (Å)	R_{\max}	Seq.	$\log T_{\max}$	Z_i/A_i
Na IX	681.72	1.171	Li	5.92	0.348
Si IX	694.90	1.151	C	6.05	0.285
Ar VIII	700.25	1.100	Na	5.61	0.175
Mg IX	706.06	1.171	Be	5.99	0.329
Fe VIII	721.26	1.049	K	5.88	0.125
Mg IX	749.55	1.171	Be	5.99	0.329
Mg VIII	762.65	1.059	B	5.91	0.288
Mg VIII	769.38	1.079	B	5.91	0.288
Ne VIII	770.42	1.171	Li	5.80	0.347
Mg VIII	772.29	1.090	B	5.91	0.288
Ne VIII	780.34	1.171	Li	5.80	0.347
Mg VIII	782.37	1.151	B	5.91	0.288
Ca IX	821.22	1.049	Mg	5.80	0.200
Mg VII	854.64	1.079	C	5.80	0.247
Mg VII	868.08	1.110	C	5.80	0.247
Ne VII	887.24	1.028	Be	5.71	0.297
Ne VII	895.16	1.100	Be	5.71	0.297
S VI	933.41	1.079	Na	5.38	0.156
Ne VII	973.33	1.028	Be	5.71	0.297
Fe X	1028.04	1.161	Cl	6.08	0.161
O VI	1031.93	1.171	Li	5.58	0.313
O VI	1037.63	1.171	Li	5.58	0.313
Si VII	1049.26	1.079	O	5.79	0.214
Al VII	1053.88	1.059	N	5.79	0.222
Al VII	1056.79	1.059	N	5.79	0.222
Al VIII	1057.86	1.069	C	5.94	0.259
Ca X	557.76	1.110	Na	5.87	0.225
Ne VI	558.59	1.028	B	5.63	0.248
Ne VI	562.80	1.028	B	5.63	0.248
Ca X	574.01	1.110	Na	5.87	0.225
Mg X	609.80	1.171	Li	6.04	0.370
N V	1238.82	1.079	Li	5.24	0.286
Fe XII	1242.00	1.141	P	6.22	0.197
N V	1242.81	1.069	Li	5.24	0.286
Mg X	624.97	1.161	Li	6.04	0.370
Si VIII	1440.51	1.028	N	5.92	0.249
Si VIII	1445.76	1.161	N	5.92	0.249
Fe XI	1467.07	1.100	S	6.14	0.179

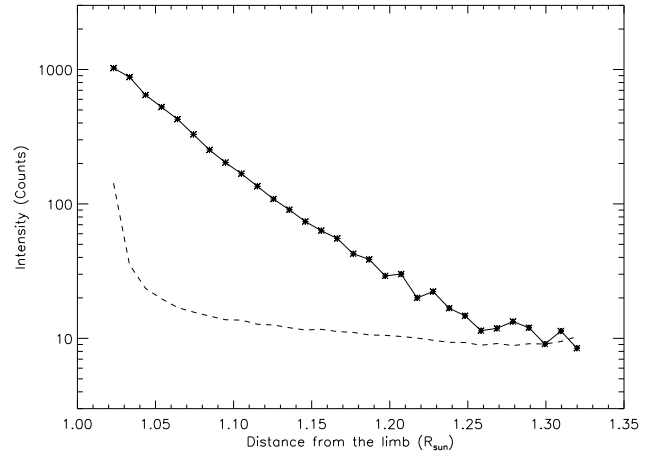


FIG. 2.— Intensity of the Mg IX 706.06 Å line as a function of distance from the limb (in counts). The scattered light intensity is superimposed as a dashed line, and it has been normalized to match the Mg IX intensity averaged over the three positions farthest from the solar limb.

3.2. Data reduction and scattered light

Raw data were reversed and corrected from flat field and geometrical distortions using the standard SUMER software available in the SolarSoft package for IDL. Corrections for deadtime and local gain depression were not necessary because count rates were always sufficiently low. A large set of lines was selected in order to sample as wide a range of Z_i/A_i ratios as possible with bright, isolated lines that minimized uncertainties tied to line profile fitting. These lines are listed in Table 1. In order to increase the signal-to-noise, the SUMER slit was divided into 10 pixel-wide bins along the slit direction: within each bin, the emission was averaged. The profile of each line was fitted with a Gaussian profile, obtaining line centroid, width and total intensity.

In the present work, we are primarily interested in line widths, but line intensities were used to determine the amount of scattered light contamination. Instrument-scattered light consists of disk radiation scattered by mirror micro-roughness, that forms on the detector a ghost, unshifted spectrum of the solar disk that contaminates true local emission. A significant scattered light blending may alter line profiles in ways that are not easy to assess and correct. Before attempting an analysis of line widths, it is important to check that the scattered light contribution is negligible and, if not negligible, to remove it. Scattered light can be distinguished from true coronal emission by considering the variations of the measured intensity with distance from the limb, because true emission decreases much faster than instrument-scattered light. In order to evaluate the amount of scattered light contaminating each line, we first determined the rate of decrease of scattered light intensity with distance from the limb. This was done first by measuring the normalized intensity versus height relationship (henceforth *scattered light profile*) of a few chromospheric and transition region lines which, outside the solar disk, are almost entirely made of scattered light. We then assumed that the emission of the selected coronal lines measured at the farthest distance from the limb is entirely composed of scattered light, and used the scattered light profile to evaluate the absolute intensity of instrument-scattered emission for each coronal line at all heights. An example of comparison between scattered light and true coronal emission is given in Figure 2 for the Mg IX line at 706.06 Å. It is impor-

tant to note that this method actually overestimates the scattered light emission. We considered the scattered light to be negligible when its intensity, as estimated using this method, is 25% or less of the measured intensity of a coronal line.

This method allowed us to determine the maximum height R_{\max} below which the scattered light can be safely considered negligible. For the strongest lines, we could stretch our measurements up to $1.17 R_{\odot}$, while only the closest bin provided intensity for the weakest lines. Table 1 also reports the value of R_{\max} for each line.

The presence of scattered light in line widths can also be checked independently by considering the quantity $d\lambda/\lambda_0$. In fact, from equation 1 it is easy to see that $d\lambda/\lambda_0$ only depends on physical properties of the ion and so it is the same for all lines of the same ion, unless some problem affects the profile of a line. We calculated this quantity for all the ions in Table 1 with more than one line in order to check whether there was agreement at all heights up to R_{\max} . In the few cases where $d\lambda/\lambda_0$ was not constant within the same ion, we have investigated the cause of the disagreement, usually due to poor signal-to-noise or to blending lines and rejected the positions where there were problems. It is important to note that ions with only one line are considered less reliable because their width $d\lambda$ could not be checked using this method.

4. ION TEMPERATURES

The ion temperatures measured from line widths are shown in Figure 3, which displays them as a function of the Z_i/A_i ratio for a few heights above the limb. The analysis method provides rather wide ranges of temperature for almost all ions, so that any height dependence is nearly washed away and the results are qualitatively the same up to the maximum height $1.17 R_{\odot}$. The ions emitting weak lines only provide a few measurements close to the limb, and in all cases they are compatible with a constant T_i value even if their T_i ranges seem to decrease with height. Brighter lines provide T_i measurements up to $1.17 R_{\odot}$, that sometimes seem to increase and sometimes seem to decrease with height; in all cases they too are compatible with constant T_i . As height increases, fewer and fewer lines are useful to measure T_i , so that it is more difficult to sample the Z_i/A_i range as accurately as with observations closer to the limb.

Landi (2008) measured the electron temperature of the same emitting plasma under consideration in the present work, finding that it is nearly isothermal at each height, with temperature slightly increasing with height from $\log(T_e/\text{K}) \simeq 5.90$ to $\log(T_e/\text{K}) \simeq 6.05$. Figure 3 shows the measured upper and lower limits of T_e on top of the T_i ranges: in all cases the latter are larger than the former and if agreement is found, it is only because the T_i ranges are rather broad. This behavior is apparent even at the lowest heights and it confirms the earlier results by Tu et al. (1998): coronal hole plasmas are not in equilibrium.

Figure 3 shows that there is a relationship between T_i and the Z_i/A_i ratio. At larger heights the number of available ions is limited so the relationship between T_i and Z_i/A_i is less apparent, or it can not even be determined, although results are consistent with those at lower heights. Figure 3 shows an U-shaped T_i versus Z_i/A_i relationship, where the ions providing large T_i at $Z_i/A_i \leq 0.2$ are Fe X to Fe XII and Ar VIII. For $Z_i/A_i > 0.2$, T_i values are more constant, showing only a mild increase with Z_i/A_i . It is interesting to note that all the ions with T_i closer to, or in agreement with, T_e all have Z_i/A_i between 0.2 and 0.3. The relationship between T_i and

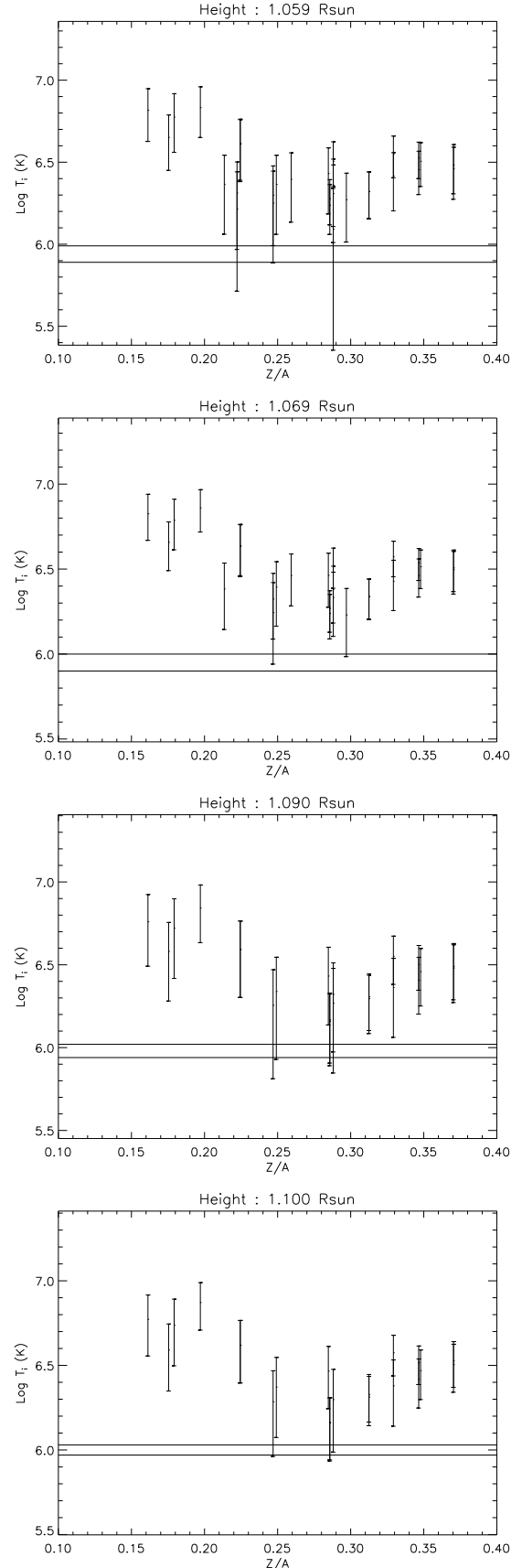


FIG. 3.— Ion temperature versus the charge-over-mass ratio Z_i/A_i , for a selected subset of measured heights. The horizontal lines represent the minimum and maximum value of the electron temperature as measured by Landi (2008).

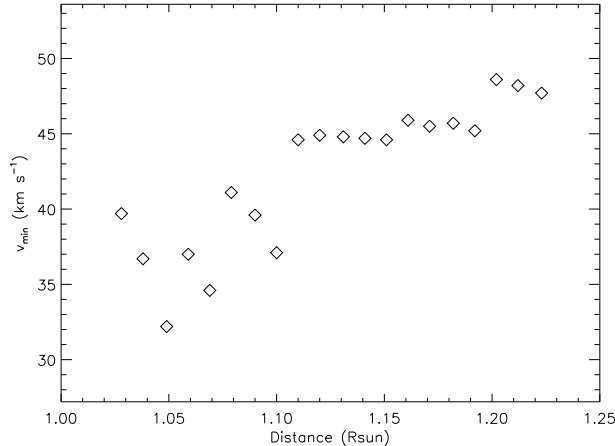


FIG. 4.— Value of v_{\min} as a function of height above the limb.

Z_i/A_i can be compared with the measurements carried out by Landi (2007) on three different quiet Sun regions using the same diagnostic method. Differences are striking, as quiet Sun T_i values show no dependence on the Z_i/A_i ratio, and they are in much better agreement with the electron temperature than in the present work. However, we found that the lines we selected have a sufficiently large signal-to-noise to provide uncertainties in the limit values of T_i that are small when compared to the range of T_i given by equation (4).

The Tu et al. (1998) diagnostic technique does not allow us to measure v_{nth} , since equation (3) only allows us to set an upper limit on it. The value of v_{\min} increases only slightly with height from $\simeq 30\text{--}35 \text{ km s}^{-1}$ to $\simeq 45\text{--}50 \text{ km s}^{-1}$, and it is shown in Figure 4.

5. THERMAL AND NON-THERMAL COMPONENTS

As discussed above, the basic assumption in the interpretation of the off-limb line profiles is that there are only two contributors to the (mainly Gaussian) widths: “thermal” microscopic motions and “non-thermal” bulk motions along the line of sight (LOS) due to unresolved waves or turbulence. Another key assumption is that the non-thermal part of the line width has no intrinsic dependence on ion charge or mass. This is valid when the spectrum is dominated by low-frequency MHD waves, but other types of dispersive waves have been suggested to play a role (e.g., Moran 2002; Ofman et al. 2005). However, we retain the standard assumption of no charge or mass dependence of the non-thermal speed, because in most models of MHD turbulence the power that resides at kinetic dispersive scales tends to be much smaller than that at the larger non-dispersive scales.

Figure 5 compares a range of observational and theoretical values for the non-thermal velocity, including the upper limits derived above. This quantity is interpreted as the transverse root mean square Alfvén wave amplitude $\langle \delta v_{\perp}^2 \rangle^{1/2}$. The wave amplitudes from theoretical models were divided by $\sqrt{2}$ in order to sample only the motions along one of the two perpendicular directions (i.e., only along the LOS). Cranmer & van Ballegoijen (2005) discussed the observational data of Banerjee et al. (1998) and Esser et al. (1999), as well as other empirical constraints on Alfvén wave properties. The discrepancy between the two theoretical model curves is due to the fact that the Cranmer & van Ballegoijen (2005) model utilized a fixed empirical set of background plasma parameters

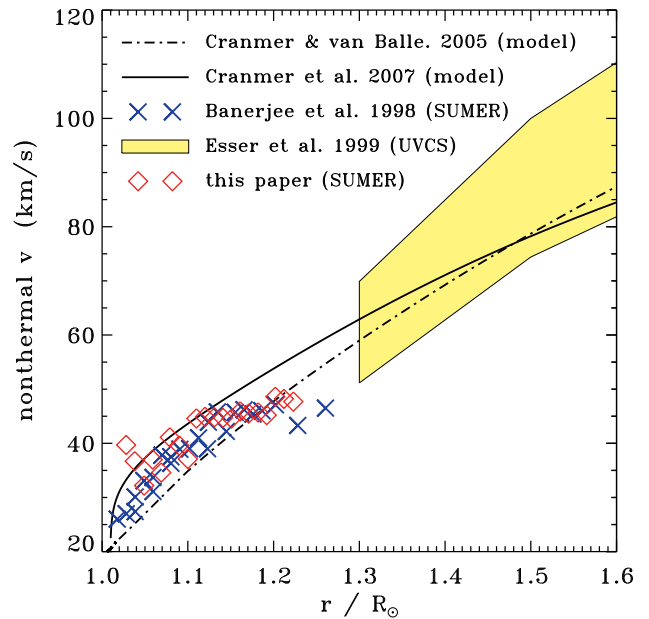


FIG. 5.— Assembled non-thermal velocities, interpreted as perpendicular Alfvén wave amplitudes and plotted versus heliocentric distance in units of the solar radius, from empirical non-WKB wave models (*dot-dashed line*; Cranmer & van Ballegoijen 2005) and turbulence-driven coronal heating models (*solid line*; Cranmer et al. 2007). Also, empirical measurements from Banerjee et al. (1998) (*blue crosses*), Esser et al. (1999) (*yellow region*), and from this paper (*red diamonds*).

(e.g., wind speed, Alfvén speed, density) and Cranmer et al. (2007) computed these properties self-consistently with the waves.

Because in coronal holes (close to the limb) the magnetic field appears to be mainly pointed in the radial direction, the LOS component of the thermal temperature (for ion i) is assumed to be identical to the perpendicular temperature $T_{\perp i}$. This assumption was validated by test calculations that took account of the full LOS integration and used anisotropic bi-Maxwellian distributions. These calculations showed that the dominant contribution to a collisional line profile (i.e., sensitive to density squared) comes from a very narrow range of heights, all close enough to the plane of the sky that the sampled component of the distribution always remained close to $T_{\perp i}$.

The model calculations below mainly utilize the ion temperature data at a single reference radius. This radius was chosen as $1.069 R_{\odot}$, which seemed to be the best balance between having a large number of available ions (which drops off as height increases) and the existence of significant “preferential heating” away from thermal equilibrium (which is lessened as height decreases). The measured maximum non-thermal speed at this height is 34.6 km s^{-1} , which falls between the modeled values of about 30 km s^{-1} (Cranmer & van Ballegoijen 2005) and 40 km s^{-1} (Cranmer et al. 2007). However, the actual non-thermal speed must be less than the upper limit derived above. Somewhat arbitrarily, we choose 25 km s^{-1} as a fiducial non-thermal speed for this height, which is used to subtract from the total line width to obtain the individual ion temperatures $T_{\perp i}$.²

² To some extent, when comparing the ion temperatures *to one another* at the same height, the assumed value for the non-thermal wave amplitude is not so important. As long as the non-thermal speed is independent of ion charge and mass, the *relative* differences between the various ion temperatures are unchanged.

6. PHYSICAL PROCESSES IN THE MODEL

The basic idea of the semi-empirical models to be discussed below is that we assume a turbulent replenishment of ion cyclotron wave power in the corona with a known radial dependence. The absolute normalization for this wave power, though, is determined for a given ion of charge Z_i and mass A_i iteratively by finding the value that produces the observed level of perpendicular heating at the reference radius of $1.069 R_\odot$. By determining this wave power for the ions, each independently of the others, we construct a model of the overall frequency dependence of the ion cyclotron power spectrum.

The solution for the radial dependence of $T_{\perp i}$ uses an internal energy conservation equation similar to that used by Cranmer et al. (1999a) with some minor changes to be discussed below. The properties of the background proton-electron plasma are held fixed at values determined by comparison with empirical measurements (mainly those of Cranmer & van Ballegooijen 2005). The heavy ions are thus treated as “test particles” that do not influence the primary plasma or one another. A dominant effect that needs to be included is the temperature equilibration due to Coulomb collisions between protons and the heavy ion species of interest. The high densities in the low corona give rise to rapid collisions that can mask the preferential ion heating from ion cyclotron waves (by driving $T_{\perp i}$ back down to the proton temperature T_p).

The time-steady energy conservation equation that we solve is given by

$$\frac{dT_{\perp i}}{dr} + \frac{T_{\perp i}}{\mathcal{A}} \frac{d\mathcal{A}}{dr} = \frac{Q_{\perp i} + C_{\perp ip}(T_{\perp p} - T_{\perp i})}{n_i u_i k_B} \quad (5)$$

where the two terms on the right-hand side represent resonant heating ($Q_{\perp i}$) and Coulomb collisions with protons ($C_{\perp ip}$). The second term on the left-hand side accounts for adiabatic expansion, and depends on the radial variation in the cross-sectional area \mathcal{A} of the polar flux tube. One notable departure from the models of Cranmer et al. (1999a) is that we do not consider the corresponding equation for the parallel ion temperature $T_{\parallel i}$. Thus, for simplicity, we assume that there is no significant dependence of $T_{\perp i}$ on $T_{\parallel i}$. Even for strong anisotropy, the isotropization (coupling) term $J_{\perp ip}$ from Cranmer et al. (1999a) is a factor of $\sim 0.2/A_i$ weaker than the standard proton-ion collision term, and thus is negligible.

The proton-ion collision coefficient in equation (5) is given by $C_{\perp ip} = 2k_B n_i \nu_{ip}$, where n_i is the ion number density. The Coulomb collision rate itself is

$$\nu_{ip} = \frac{16}{3} \pi^{1/2} \ln \Lambda \frac{q_i^2 q_p^2 n_p}{m_i m_p a_{\parallel} a_{\perp}^2} \quad (6)$$

(e.g., Spitzer 1962), and

$$a_{\parallel} \equiv \left[(2k_B T_{\parallel i} / m_i) + (2k_B T_{\parallel p} / m_p) \right]^{1/2} \quad (7)$$

$$a_{\perp} \equiv \left[(2k_B T_{\perp i} / m_i) + (2k_B T_{\perp p} / m_p) \right]^{1/2} \quad (8)$$

(see also Barakat & Schunk 1981, 1982; Isenberg 1984). As in Cranmer et al. (1999a), we take the Coulomb logarithm to be a constant of $\ln \Lambda = 21$. We assume the protons are isotropic, and we also set $T_{\parallel i} = T_p$ in the definition of a_{\parallel} (which was verified to hold at the SUMER heights in trial runs using the original equations from Cranmer et al. 1999a). We do not consider collisional interactions between ion species i and any other heavy ion species, which implies that ion i does not ionize or recombine to any other charge states over the range of heights (see, e.g., Lie-Svendsen & Esser 2005).

The resonant cyclotron heating rate is given in the so-called “optically thin” (narrow resonance zone) limit of Cranmer (2000) as

$$\frac{Q_{\perp i}}{m_i n_i} = \frac{4\pi^2 \mathcal{P}(\Omega_i, r)}{B_0^2} \Omega_i^2 V_A^2 \left(1 - \frac{Z_i}{A_i} \right) \quad (9)$$

where B_0 is the radial background magnetic field strength, Ω_i is the ion gyrofrequency, and V_A is the Alfvén speed. The resonant wave power spectrum $\mathcal{P}(\omega)$ differs from the power spectrum used by Cranmer et al. (1999a) by a factor of 4π because the latter was defined as the spectrum of the total magnetic fluctuation variance $\langle \delta B_{\perp}^2 \rangle$. $\mathcal{P}(\omega)$, however, is defined as the spectrum of the total fluctuation energy density (see eqs. [15] and [22] below).

Cranmer et al. (1999a) assumed that the power spectrum scaled with the overall radial dependence of $\langle \delta B_{\perp}^2 \rangle$, as computed via MHD wave action conservation. However, the relatively small amount of energy in the high-frequency tail of the spectrum may not necessarily scale with the total integrated power. Thus, here we modify this radial dependence using the MHD turbulence theory of Cranmer & van Ballegooijen (2003) to take account of an assumed anisotropic cascade that maintains the high-frequency tail. We assume that $\mathcal{P}(\Omega_i, r)$ is a separable function of radius and frequency (for which $\omega \approx \Omega_i$). The radial dependence is given by

$$\mathcal{P}(\Omega_i, r) \propto \frac{V_A^{3/2}}{\rho^{1/2} (u_p + V_A)^3}, \quad (10)$$

where ρ is the mass density. This scaling relation is derived in Section 7 below, and the normalization constant to be used is the main adjustable parameter that we modify to produce agreement with the measured values of $T_{\perp i}$ at $1.069 R_\odot$.

The background plasma properties are given by the empirical model of Cranmer & van Ballegooijen (2005). These properties include the polar flux-tube area $\mathcal{A}(r)$, the outflow speeds (for which we assume that the ions are flowing at the same speed as the protons; $u_i = u_p$), and the number densities. The primary plasma number density ($n_p \approx n_e$) is assumed to have the same radial dependence as the ion number density n_i . Note that the absolute value of the ion number density is never needed, only its radial dependence.

The Cranmer & van Ballegooijen (2005) model was essentially a “cold plasma” treatment, so our description of the background proton temperature T_p is given by scaling the self-consistent polar coronal hole temperature of Cranmer et al. (2007) up and down by arbitrary constant factors. The location of the transition region was also scaled down to a standard height of $0.003 R_\odot$ above the photosphere. We assume isotropic protons with $T_{\parallel p} = T_{\perp p} \equiv T_p$. The actual proton temperature in the corona is not well constrained by observations, since line ratio techniques are sensitive to the electron temperature, and the widths of H^0 lines are more strongly “contaminated” by non-thermal motions than the lines of heavy ions.

In order to determine what to use for the proton temperature in the models, Figure 6 shows a range of measurements and model predictions for T_p , as well as the electron temperature T_e (which is expected to be collisionally coupled to the protons at high enough densities) and the mean one-fluid temperature, which should be approximately proportional to $(T_p + T_e)/2$. Off-limb measurements of T_e in polar coronal holes are shown from SUMER data described by Wilhelm (2006) and Landi (2008). Proton temperatures at large heights have been measured by UVCS/SOHO, and the plotted points

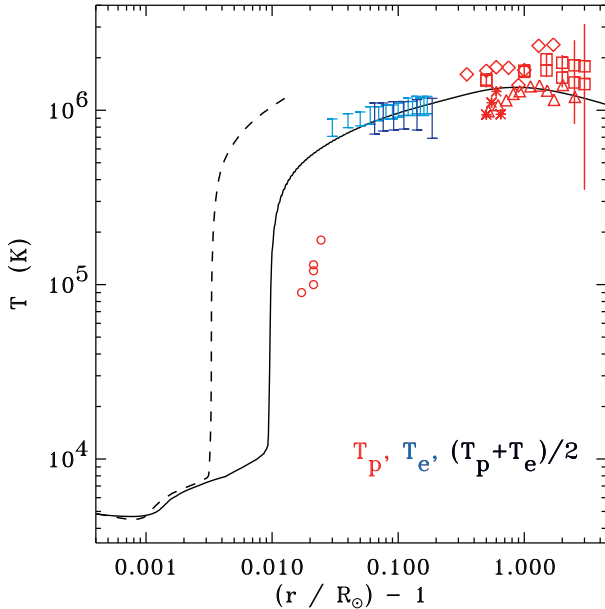


FIG. 6.— Assembled temperatures in polar coronal holes: Mean plasma temperatures from a semi-empirical VAL/FAL-type model (*dashed line*; Avrett & Loeser 2008) and from a turbulence-driven coronal heating model (*solid line*; Cranmer et al. 2007). T_e from off-limb SUMER measurements made by Wilhelm (2006) (*dark blue bars*) and Landi (2008) (*light blue bars*). T_p from off-limb SUMER measurements by Marsch et al. (2000) (*circles*), and UVCS measurements assembled by Cranmer (2004), with data from Cranmer et al. (1999b) (*squares*), Esser et al. (1999) (*diamonds*), Zangrilli et al. (1999) (*asterisks*), and Antonucci et al. (2000) (*triangles*).

are those assembled by Cranmer (2004), with a model prediction for the non-thermal wave amplitudes subtracted from the empirical kinetic temperatures. The transition-region-like values of T_p at low heights were measured by Marsch et al. (2000); these are quite low compared to most time-steady coronal models that place the sharp transition region at a lower height around $\approx 0.003 R_\odot$. These observations may have been influenced by the prevalence of narrow and cool spicules above the limb and may not be representative of the coronal footpoints of solar wind streams.

Before proceeding to discuss the solution of equation (5), it is important to make clear the relative strengths of the individual heating and cooling terms in this conservation equation. As an illustration, Figure 7 shows the radial dependence of *timescales* computed from each term in equation (5) for the standard choice of parameters (and the O^{5+} ion) discussed in § 8. Given that the terms in this equation have the units of a spatial temperature gradient, a timescale can be constructed by multiplying by the quantity $u_i/T_{\perp i}$ and taking the inverse. For example, the timescale corresponding to ion cyclotron heating is given by

$$\tau_{\text{heat}} = \frac{n_i k_B T_{\perp i}}{Q_{\perp i}}. \quad (11)$$

The timescale for adiabatic cooling τ_{adia} is given by using the second term on the left-hand side of equation (5). Two timescales for Coulomb collisions can be constructed by using either the ion temperature (i.e., the final term in eq. [5]) or the proton temperature (the penultimate term). These generate the collisional timescales $\tau_{\text{coll},i}$ and $\tau_{\text{coll},p}$, respectively. As can be seen from Figure 7, at low heights the most rapid processes are the Coulomb collisions. Above a height of approximately $0.1 R_\odot$, the ion cyclotron heating timescale begins to be as rapid as collisions, and the ion temperature $T_{\perp i}$ begins to

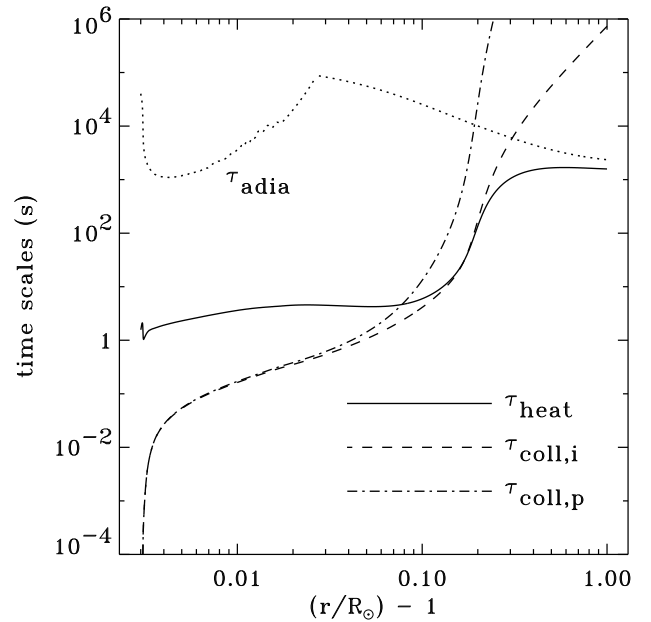


FIG. 7.— Radial dependence of timescales corresponding to individual terms in the energy conservation equation (5); see text for definitions.

increase above the proton temperature. At still larger heights in the extended corona ($r \approx 2R_\odot$) adiabatic cooling begins to be as important as ion cyclotron heating, and Coulomb collisions are unimportant.

The numerical integration technique used to compute $T_{\perp i}(r)$ from equation (5) was slightly different from that used by Cranmer et al. (1999a). Because of the strong collisions near the coronal base, the earlier use of simple Euler steps became highly unstable for realistic grid spacings. Instead, we used a piecewise analytic solution of the energy equation that takes account of the collisional coupling explicitly. Equation (5) can be expressed schematically as

$$\frac{dT_{\perp i}}{dr} + pT_{\perp i} = q \quad (12)$$

where p and q are considered to be slowly varying functions of radius. The Coulomb collision term has been split up between p and q . The analytic solution of this equation, which we use to step the solution for $T_{\perp i}$ up from height r_j to height r_{j+1} , is given by the integrating factor method as

$$T_{\perp i,j+1} = \frac{q}{p} + e^{-p(r_{j+1}-r_j)} \left(T_{\perp i,j} - \frac{q}{p} \right). \quad (13)$$

In the limit of weak collisions ($p \ll 1$), this reduces to the standard Euler step,

$$T_{\perp i,j+1} \approx T_{\perp i,j} + q(r_{j+1} - r_j). \quad (14)$$

In the limit of strong collisions (i.e., ignoring the adiabatic expansion and cyclotron heating terms), the ratio q/p reduces to the proton temperature T_p , and equation (13) is seen to stably drive the solution towards thermal equilibrium.

7. EXPECTATIONS FROM ANISOTROPIC TURBULENCE THEORY

As an independent prediction of the resonant wave power, we aim to describe the anisotropic evolution of wave energy in 2D wavenumber space (k_{\parallel}, k_{\perp}) by means of the advection-diffusion theory described by Cranmer & van Ballegoijen (2003) and in Appendix C of Cranmer & van Ballegoijen (2005). The theoretical development given in this section is

somewhat independent of the “semi-empirical” derivation of wave power that comes from solving the equations of the previous section.

The goal is to develop an analytic solution for the turbulent power spectrum (for frequencies near the ion cyclotron resonances) in the limit that the cascade is allowed to proceed to its final “driven” steady state in a small homogeneous volume of plasma. The three-dimensional total power spectrum is defined as

$$\int d^3\mathbf{k} P_{3D}(\mathbf{k}) = U_{\text{tot}} \approx \frac{\langle \delta B_{\perp}^2 \rangle}{4\pi} \quad (15)$$

where U_{tot} is the total energy density of the Alfvén waves, and we write the volume element $d^3\mathbf{k}$ in cylindrical coordinates as $2\pi k_{\perp} dk_{\perp} dk_{\parallel}$ to assume symmetry in the two directions perpendicular to the background field.

For fully developed anisotropic MHD turbulence, we assume the power spectrum to be a separable function of two variables: k_{\perp} and a nonlinearity parameter y defined as the ratio of the local wind-frame frequency $V_A k_{\parallel}$ to an assumed nonlinear eddy turnover rate $\langle \delta V \rangle k_{\perp}$ (see, e.g., Goldreich & Sridhar 1995). We use the notation from Section 2.3 of Cranmer & van Ballegoijen (2003) and define

$$P_{3D}(k_{\parallel}, k_{\perp}) = \frac{\rho V_A W_{\perp}^{1/2}}{k_{\perp}^3} g(y) \quad (16)$$

where $W_{\perp}(k_{\perp})$ is a reduced power spectrum that describes the dominant perpendicular cascade. For the MHD inertial range, the reduced spectrum is given as

$$W_{\perp}(k_{\perp}) = \begin{cases} U_{\text{tot}}(k_{\perp}/k_{\text{out}})^{-2/3} (3\pi\rho)^{-1}, & k_{\text{out}} < k_{\perp} < k_{\text{in}} \\ 0, & \text{otherwise} \end{cases} \quad (17)$$

The above definition assumes the existence of a finite outer-scale perpendicular wavenumber k_{out} , which we assumed to be inversely proportional to the correlation length of the turbulence, and an inner-scale wavenumber $k_{\text{in}} \gg k_{\text{out}}$, which we assume to be equivalent to the inverse proton gyrofrequency. The factor of $3\pi\rho$ above is needed to normalize the full power spectrum as defined in eq. (15).

The k_{\parallel} dependence of the power spectrum is contained in the dimensionless $g(y)$ function given in eq. (16). We define

$$y = \frac{k_{\parallel} V_A}{k_{\perp} W_{\perp}^{1/2}}. \quad (18)$$

The condition $y = 1$ is defined as “critical balance” by Goldreich & Sridhar (1995), and their analysis only constrains the general shape of $g(y)$, not its exact value. The critical balance condition captures the highly nonlinear state of turbulence, for which a coherent wave survives for no more than about one or two periods before nonlinear processes transfer its energy to the smaller scales. Cranmer & van Ballegoijen (2003) solved a simple wavenumber diffusion equation to obtain an analytic relation for $g(y)$. For the MHD inertial range, this relation can be shown to be equivalent to

$$g(y) = \frac{2\Gamma(n)}{3\Gamma(n-0.5)\sqrt{\pi}} \left(1 + \frac{4y^2}{9}\right)^{-n} \quad (19)$$

which is normalized to unity when integrated over all y , and with

$$n = 1 + \frac{3\beta}{4\gamma}. \quad (20)$$

The dimensionless constants β and γ describe the relative strengths of advection and diffusion, respectively, in the k_{\perp} direction. They only occur as the ratio β/γ , which we take to be a free parameter. Cranmer & van Ballegoijen (2003) discussed the most realistic values for this ratio, which is relatively unconstrained by existing turbulence simulations. The “random walk” turbulence model of van Ballegoijen (1986), though, suggested that $\beta/\gamma \approx 1$. However, Cranmer & van Ballegoijen (2003) found that one would need this ratio to be smaller than about 0.25 in order to produce enough parallel cascade in the corona to heat protons and heavy ions via cyclotron resonance.

With the above definitions it becomes possible to integrate over k_{\perp} and obtain a reduced 1D power spectrum

$$P_{1D}(k_{\parallel}) = 2\pi \int_{k_{\text{out}}}^{k_{\text{in}}} dk_{\perp} k_{\perp} P_{3D}(k_{\parallel}, k_{\perp}) \quad (21)$$

which is related to the frequency spectrum $\mathcal{P}(\omega)$ via

$$P_{1D}(k_{\parallel}) dk_{\parallel} = \mathcal{P}(\omega) d\omega. \quad (22)$$

If we assume, for simplicity, that the ion cyclotron waves of interest are far enough from the proton resonance for the standard MHD dispersion relation ($\omega = k_{\parallel} V_A$) to hold, the above parameterizations for $P_{3D}(k_{\parallel}, k_{\perp})$ can be applied to show that

$$\mathcal{P}(\omega) = \sqrt{\frac{4\pi\rho U_{\text{tot}}}{3}} k_{\text{out}}^{1/3} \int_{k_{\text{out}}}^{k_{\text{in}}} dk_{\perp} \frac{g(y)}{k_{\perp}^{7/3}}. \quad (23)$$

This equation, combined with the cyclotron resonant frequency condition

$$\omega - u_i k_{\parallel} - \Omega_i = 0, \quad (24)$$

is used to produce the “theoretical” power spectra (as a function of the β/γ parameter) that are compared with the empirically derived power spectra at $1.069 R_{\odot}$. For ion cyclotron waves at any given height in the low corona (where $u_i \ll V_A$), the wave frequency ω is directly proportional to the ion charge to mass ratio Z_i/A_i . The main plasma quantities, including the Alfvén wave scale lengths k_{out} and k_{in} , the total energy density U_{tot} , and the ion Larmor frequencies Ω_i , are taken from the radially dependent coronal hole model of Cranmer & van Ballegoijen (2005).

The above equations specify how the resonant frequency spectrum $\mathcal{P}(\omega)$ can be computed, but it is also helpful to derive a concise relation for the large-scale radial dependence of the wave power in the ion cyclotron frequency range. The gyroresonant wave power exists in the limit of large values of the dimensionless critical-balance parameter y . For $y \gg 1$, the function $g(y) \propto y^{-2n}$, and this implies that the high-frequency tail of the spectrum has a similar power-law dependence $\mathcal{P} \propto \omega^{-2n}$. Cranmer et al. (1999) treated this exponent as a free parameter η . Utilizing the definitions given above, this proportionality can be expressed in terms of more basic plasma parameters as

$$g(y) \propto k_{\perp}^{4n/3} \left(\frac{k_{\text{out}}^{2/3} U_{\text{tot}}}{3\pi\rho\Omega_i^2} \right)^n. \quad (25)$$

Note that the actual frequency dependence is “hidden” in in the ion gyrofrequency Ω_i , which is simply Z_i/A_i times the proton gyrofrequency Ω_p . Performing the integration in equation (23) and removing all constants thus provides the radial dependence of the power spectrum:

$$\mathcal{P} \propto \frac{\rho^{0.5-n} U_{\text{tot}}^{n+0.5} k_{\text{out}}^{(2n+1)/3}}{\Omega_p^{2(n+2)/3} w_p^{4(n-1)/3}} \quad (26)$$

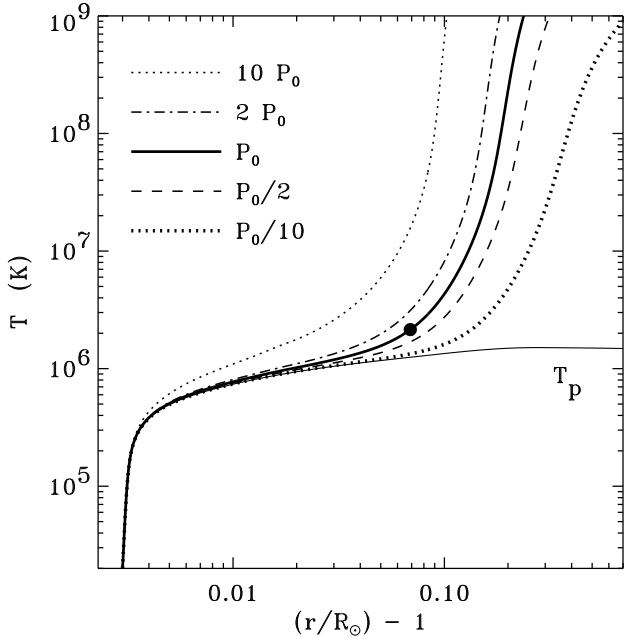


FIG. 8.— Radial dependence of modeled proton temperature (*thin solid line*) and perpendicular O^{5+} temperatures, assuming a range of resonant wave power normalization values given relative to P_0 , the iterated value required to heat the ions to the observed level at $1.069 R_\odot$ (*thick solid line*). Resulting values for $T_{\perp i}(r)$ for power levels of $10P_0$ (*thin dotted line*), $2P_0$ (*dot-dashed line*), $0.5P_0$ (*dashed line*), and $0.1P_0$ (*thick dotted line*) are also shown.

where the proton thermal speed w_p is part of the definition of the mean proton gyroradius used in k_{in} . Also, the constant ratio of Z_i/A_i has been removed in order to isolate the radial dependence for any given ion resonance.

We will see below that the limiting case of $\beta/\gamma \ll 1$ (i.e., $n \approx 1$, or $\eta \approx 2$ in the notation of Cranmer et al. 1999) may be appropriate for comparison with the observations, so let us apply this limit to obtain

$$\mathcal{P} \propto \rho^{-1/2} U_{tot}^{3/2} k_{out} \Omega_p^{-2}. \quad (27)$$

The outer scale wavenumber k_{out} is usually assumed to be the reciprocal of the perpendicular correlation length, and the latter is often taken to be proportional to the flux-tube cross section, so we assume $k_{out} \propto A^{-1/2} \propto B_0^{1/2}$ (Hollweg 1986). We also know that $\Omega_p \propto B_0$. Finally, the total Alfvén wave energy density can be assumed to scale with the WKB conservation of wave action, which is given by

$$U_{tot} \propto \frac{V_A}{\mathcal{A}(u_p + V_A)^2}. \quad (28)$$

Applying these scalings then leads to the radial dependence for the resonant power given in equation (10).

8. MODEL RESULTS

The semi-empirical equation of ion energy conservation (eq. [5]) was integrated numerically from the coronal base ($1.003 R_\odot$) to the reference radius of $1.069 R_\odot$ for each of 25 ions having measured SUMER line widths at this height. These ions have Z_i/A_i values ranging between 0.161 (Fe^{9+}) and 0.370 (Mg^{9+}), and ion temperatures between 1.69 MK (Ne^{6+}) and 7.22 MK (Fe^{11+}). Also, several grids of models were created for a range of proton temperatures, all with the same relative radial dependence but with values at $1.069 R_\odot$ ranging between 0.5 and 3 MK.

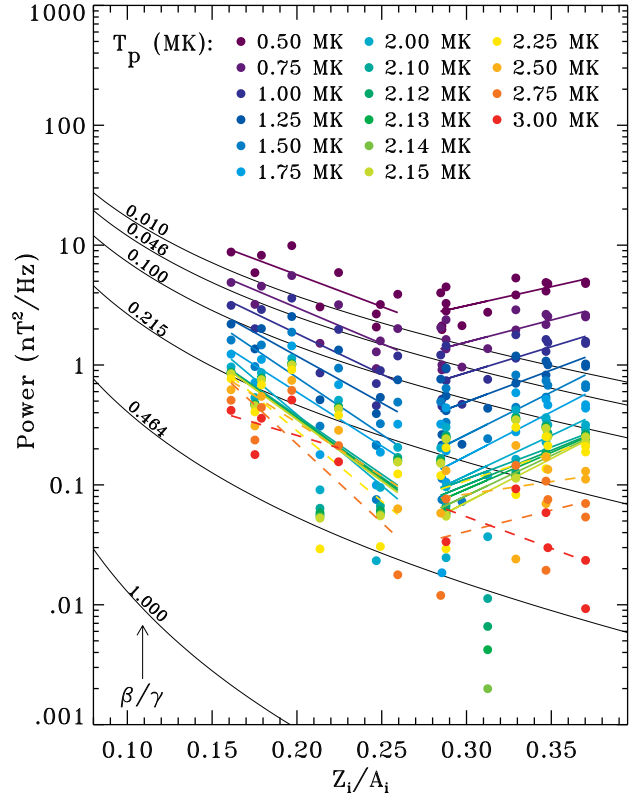


FIG. 9.— Ion cyclotron wave power at $1.069 R_\odot$ plotted versus ion charge-to-mass ratio Z_i/A_i (the latter a proxy for frequency). Empirically determined wave power levels for individual ions (*filled circles*; see color key for T_p normalization) are compared with theoretical predictions for the wave power, based on adopted radially dependent models of the total wave power, Alfvén speed, and other plasma properties (*black solid curves*).

Figure 8 illustrates the result of this numerical integration for a representative ion (O^{5+}) and a specific choice for the proton temperature. The optimal (iterated) wave power necessary to heat these ions to the observed temperature at the reference height is denoted P_0 . Figure 8 also shows the resulting $T_{\perp i}(r)$ curves that are obtained when P_0 is varied up and down by factors of 2 to 10. The ion temperature can become several orders of magnitude larger than the proton temperature at larger heights. This has been confirmed by the UVCS O VI measurements between 1.5 and $3.5 R_\odot$ (e.g., Kohl et al. 2006; Cranmer et al. 2008). Note, though, that at such large heights, where Coulomb collisions become very weak, a more proper treatment of the resonant wave-particle interactions is warranted—either via the coupled $T_{\perp i}$ and $T_{\parallel i}$ equations (Cranmer et al. 1999a) or even a fully kinetic treatment of the ion velocity distributions (e.g., Isenberg & Vasquez 2007).

Figure 9 shows the result of repeating the numerical integration and wave-power iteration for all 25 ions at $1.069 R_\odot$. Recall that *no assumptions* were made about the frequency dependence of the resonant wave power spectrum for these models. The power for each ion was computed independently of the others. The resonant wave power is shown as a function of Z_i/A_i for each of the 16 choices for the T_p normalization. Straight-line fits are shown for two distinct regions of Z_i/A_i values, in order to guide the eye and make rough comparisons to the theoretical expectations for $\mathcal{P}(\omega)$. The black curves in Figure 9 are shown to compare the semi-empirical results with the expectations of turbulence theory. In other words, these curves come from evaluating equation (23) numerically for $\mathcal{P}(\omega)$, assuming a range of β/γ values between 0.01 and

1.

For large enough choices for T_p , there occur several ions that have smaller perpendicular temperatures than the adopted proton temperature at $1.069 R_\odot$. These are shown with dashed lines for the straight-line fits, and thus should not be considered as self-consistent models for the entire ion data set. In Figure 9, the “green” curves indicate a collection of models all with $T_p \approx 2.1$ MK, because we wanted to explore specifically the behavior of the O^{5+} heating in the limit of strong collisionality (i.e., because $T_{\perp i} \approx 2.15$ MK for this ion); see below.

For the lowest frequencies (i.e., $Z_i/A_i \lesssim 0.27$), both the spectral slope and the absolute wave power at $1.069 R_\odot$ seem to agree well with the turbulent cascade predictions for values of $\beta/\gamma \lesssim 0.3$. This agreement is actually quite notable, since the theoretical predictions (black curves) were normalized by pre-existing assumptions about, e.g., the total wave power U_{tot} , and the empirical sets of points were iterated completely independently from any considerations of MHD turbulence. If the proton temperature in the low corona remains less than about 2 MK (see, e.g., Figure 6), then this result provides some additional observational justification for a value of β/γ of order 0.1 to 0.3 (see Cranmer & van Ballegoijen 2003).

For the highest frequencies ($Z_i/A_i \gtrsim 0.27$), it seems clear that some kind of “upswing” in the resonant wave power is indicated by the empirical points in Figure 9. If this is indeed a real effect, there are several possible explanations in terms of MHD and kinetic fluctuations:

1. The additional power at large gyrofrequencies may arise because of *plasma instabilities* centered around the cyclotron resonances of alpha particles ($Z_i/A_i = 0.5$) or protons ($Z_i/A_i = 1$); see, e.g., Markovskii (2001), Isenberg (2001), Zhang (2003), Laming (2004), and Markovskii et al. (2006). Thus, the effects seen at charge-to-mass ratios around 0.35 may just be the tail of an additional population of waves that peak at larger frequencies.
2. This may be a similar effect as the spectral flattening (i.e., enhancement above a power law frequency dependence) evident in radio scintillation measurements of density fluctuations at larger heights (e.g., Coles & Harmon 1989). This flattening was modeled successfully by Harmon & Coles (2005) by taking into account the enhanced compressibility of *obliquely propagating Alfvén waves* once they reach ion cyclotron frequencies. It may be possible for compressibility effects to either alter some aspects of the turbulent cascade or change the functional dependence of the heating rate on the available wave power (i.e., eq. [9]) in order to produce this effect.
3. A somewhat more speculative idea is that the particular type of MHD turbulence acting in the low corona may undergo a kind of *bottleneck effect* where the wave power piles up near the dissipation range. This effect appears in many turbulence simulations, and it has often been suspected of being numerical in origin (e.g., Verma & Donzis 2007). However, there have been independent theoretical predictions of similar kinds of wave-power pileup arising from nonlocal interactions between disparate scales in k -space (e.g., Falkovich 1994; Biskamp et al. 1998).

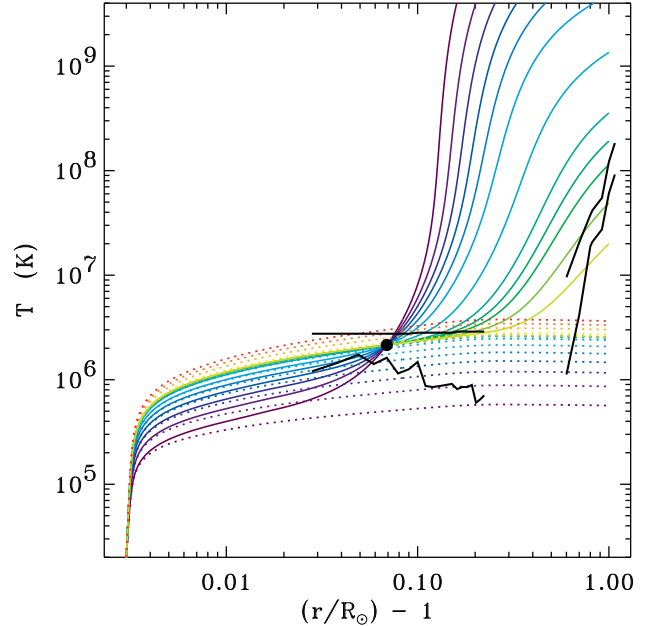


FIG. 10.— Radial dependence of modeled proton temperatures (*dotted lines*) and perpendicular O^{5+} temperatures (*solid lines*), with the same color key as Figure 9. Also shown are observational lower and upper limits on $T_{\perp i}$ from SUMER and UVCS (*black solid lines*).

Figure 10 illustrates the radial dependence of the ion heating for O^{5+} ions, and shows how $T_{\perp i}$ varies with the different choices for T_p . The color scheme for proton temperature values is the same as in Figure 9. The black curves at the heights corresponding to the SUMER measurements show the lower and upper limits defined by equation (4). The black curves at larger heights give the limits on the ion temperature from recent UVCS $O\text{ VI}$ empirical models (Cranmer et al. 2008).

The models with relatively low proton temperatures ($T_p \lesssim 2$ MK) require a large amount of resonant wave power to “combat” Coulomb collisions and raise the ion temperature to the observed SUMER value at $1.069 R_\odot$. Unfortunately, this large resonant wave power then causes the ion temperature to “explode” to unrealistically huge values at larger heights where the plasma becomes collisionless. On the other hand, the green curves in Figure 10 agree reasonably well with both the SUMER and UVCS data and correspond to larger assumed values for T_p . Here, the reason for a fine grid of proton temperature curves having

$$0 < \frac{T_{\perp i}}{T_p} - 1 \ll 1 \quad (29)$$

becomes evident. These choices for T_p do not need as much wave power to reach the observed SUMER ion temperature at $1.069 R_\odot$, and thus they are less likely to result in unrealistically large temperatures at larger heights. However, it is important to note that these best-fitting solutions seem to have quite strong Coulomb collisions even at the *lowest* of the SUMER heights.³ This would imply that at, say, 1.03 – $1.05 R_\odot$, all of the ion temperatures would be expected to be tightly coupled to both T_p and to one another. This, as seen in Figure 3 above, is not the case. Clearly the models presented

³ It is possible, of course, that Coulomb collisions are not the only means of thermalizing and isotropizing the ions. The existence of various kinds of turbulent fluctuations has been suggested to be able to couple particles and possibly provide extra “quasi-collisions” (e.g., Perkins 1973; Dum 1983; Kellogg 2000). This may need to be investigated in the context of the low corona.

here are only a first step toward a self-consistent description of the preferential ion heating that applies for the full range of heights observed by SUMER and UVCS.

9. CONCLUSIONS

In the present work we have used SUMER observations of a polar coronal hole to measure the ion temperatures T_i for a large number of ions, in order to determine their dependence on the charge-over-mass ratio Z_i/A_i . We repeated our measurements for several heights between $1.03 R_\odot$ and $1.17 R_\odot$ in order to investigate the height dependence of our results. We used the method devised by Tu et al. (1998) to determine T_i ; this method only assumed that non-thermal velocities v_{nth} are the same for all ions.

We found that ion temperatures are larger than the electron temperatures in nearly all cases and at all heights, and that results are qualitatively the same in the $1.03\text{--}1.17 R_\odot$ range of distances from the limb, although the number of available ions decreases as distance from the limb increases. Our most notable result is an U-shaped dependence of T_i from Z_i/A_i , where ions with low Z_i/A_i (less than about 0.23) have very large T_i values, while those with $Z_i/A_i \gtrsim 0.23$ have roughly constant T_i .

We used our measured T_i values to constrain an exploratory model of solar wind heating and acceleration based on ion-

cyclotron waves, under the assumption that such waves are gradually replenished as they are dissipated. The measured T_i values help us constrain the proton temperatures as well as the ratio between advection and diffusion (in a likely scenario of anisotropic MHD turbulence). We find that the observations of ions having Z_i/A_i values smaller than about 0.25 are consistent with a turbulence model very similar to that shown by Cranmer & van Ballegoijen (2003) to be able to energize protons in the extended corona.

However, T_i measurements obtained for ions with Z_i/A_i larger than 0.25 show an upswing in wave power that is difficult to reconcile with traditional views of turbulent cascade. We discuss the implications of this inferred increase in wave power, suggesting several different possibilities such as plasma instabilities, obliquely propagating Alfvén-wave compressibility effects, or a turbulent bottleneck effect.

The work of Enrico Landi is supported by the NNG06EA14I, NNH06CD24C as well as other NASA grants. The work of Steven Cranmer is supported by NASA under grants NNX06AG95G and NNG04GE77G to the Smithsonian Astrophysical Observatory. The authors would like to thank Adriaan van Ballegoijen and Mari Paz Miralles for valuable discussions.

REFERENCES

- Abraham-Shrauner, B., & Feldman, W. C. 1977, *J. Geophys. Res.*, 82, 618
 Antonucci, E., Doderio, M. A., & Giordano, S. 2000, *Sol. Phys.*, 197, 115
 Avrett, E. H., & Loeser, R. 2008, *ApJS*, 175, 229
 Axford, W. I., & McKenzie, J. F. 1992, in *Solar Wind Seven*, ed. E. Marsch & R. Schwenn (New York: Pergamon), 1
 Banerjee, D., Teriaca, L., Doyle, J. G., & Wilhelm, K. 1998, *A&A*, 339, 208
 Barakat, A. R., & Schunk, R. W. 1981, *J. Phys. D*, 14, 421
 Barakat, A. R., & Schunk, R. W. 1982, *Plasma Phys.*, 24, 389
 Biskamp, D., Schwarz, E., & Celani, A. 1998, *Phys. Rev. Lett.*, 81, 4855
 Chandran, B. D. G. 2005, *Phys. Rev. Lett.*, 95, 265004
 Coles, W. A., & Harmon, J. K. 1989, *ApJ*, 337, 1023
 Cranmer, S. R. 2000, *ApJ*, 532, 1197
 Cranmer, S. R. 2001, *J. Geophys. Res.*, 106, 24937
 Cranmer, S. R. 2002, *Space Sci. Rev.*, 101, 229
 Cranmer, S. R. 2004, in *SOHO-15: Coronal Heating*, ed. R. W. Walsh, J. Ireland, D. Danesy, & B. Fleck (Noordwijk, The Netherlands: ESA), ESA SP-575, 154
 Cranmer, S. R., Field, G. B., & Kohl, J. L. 1999a, *ApJ*, 518, 937
 Cranmer, S. R., Panasyuk, A. V., & Kohl, J. L. 2008, *ApJ*, 678, 1480
 Cranmer, S. R., & van Ballegoijen, A. A. 2003, *ApJ*, 594, 573
 Cranmer, S. R., & van Ballegoijen, A. A. 2005, *ApJS*, 156, 265
 Cranmer, S. R., van Ballegoijen, A. A., & Edgar, R. J. 2007, *ApJS*, 171, 520
 Cranmer, S. R., et al. 1999b, *ApJ*, 511, 481
 Dolla, L., & Solomon, J. 2008, *A&A*, 483, 271
 Dum, C. T. 1983, in *Solar Wind Five*, ed. M. Neugebauer, NASA CP-2280, 369
 Esser, R., Fineschi, S., Dobrzycka, D., Habbal, S. R., Edgar, R. J., Raymond, J. C., Kohl, J. L., & Guhathakurta, M. 1999, *ApJ*, 510, L63
 Falkovich, G. 1994, *Phys. Fluids*, 6, 1411
 Goldreich, P., & Sridhar, S. 1995, *ApJ*, 438, 763
 Harmon, J. K., & Coles, W. A. 2005, *J. Geophys. Res.*, 110, A03101
 Hollweg, J. V. 1986, *J. Geophys. Res.*, 91, 4111
 Hollweg, J. V. 2000, *J. Geophys. Res.*, 105, 7573
 Hollweg, J. V., & Isenberg, P. A. 2002, *J. Geophys. Res.*, 107 (A7), 1147
 Hollweg, J. V., & Turner, J. M. 1978, *J. Geophys. Res.*, 83, 97
 Isenberg, P. A. 1984, *J. Geophys. Res.*, 89, 6613
 Isenberg, P. A. 2001, *J. Geophys. Res.*, 106, 29249
 Isenberg, P. A., & Hollweg, J. V. 1983, *J. Geophys. Res.*, 88, 3923
 Isenberg, P. A., & Vasquez, B. J. 2007, *ApJ*, 668, 546
 Kellogg, P. J. 2000, *ApJ*, 528, 480
 Kohl, J. L., Noci, G., Cranmer, S. R., & Raymond, J. C. 2006, *A&A Rev.*, 13, 31
 Laming, J. M. 2004, *ApJ*, 604, 874
 Landi, E. 2007, *ApJ*, 663, 1363
 Landi, E. 2008, *ApJ*, in press
 Lie-Svendsen, Ø., & Esser, R. 2005, *ApJ*, 618, 1057
 Markovskii, S. A. 2001, *ApJ*, 557, 337
 Markovskii, S. A., Vasquez, B. J., Smith, C. W., & Hollweg, J. V. 2006, *ApJ*, 639, 1177
 Marsch, E., Goertz, C. K., & Richter, K. 1982, *J. Geophys. Res.*, 87, 5030
 Marsch, E., Tu, C.-Y., & Wilhelm, K. 2000, *A&A*, 359, 381
 Moran, T. G. 2002, *BAAS*, 34, 790 (abstract 88.05)
 Ofman, L., Davila, J. M., Nakariakov, V. M., & Viñas, A.-F. 2005, *J. Geophys. Res.*, 110, A09102
 Perkins, F. 1973, *ApJ*, 179, 637
 Ruzmaikin, A., & Berger, M. A. 1998, *A&A*, 337, L9
 Seely, J.F., Feldman, U., Schühle, U., Wilhelm, K., Curdt, W., & Lemaire, P. 1997, *ApJ*, 484, L87
 Spitzer, L., Jr. 1962, *Physics of Fully Ionized Gases*, 2nd ed. (New York: Wiley)
 Tu, C.-Y., & Marsch, E. 1997, *Sol. Phys.*, 171, 363
 Tu, C.-Y., Marsch, E., Wilhelm, K., & Curdt, W. 1998, *ApJ*, 503, 475
 van Ballegoijen, A. A. 1986, *ApJ*, 311, 1001
 Verma, M. K., & Donzis, D. 2007, *J. Phys. A*, 40, 4401
 Wilhelm, K. 2006, *A&A*, 455, 697
 Wilhelm, K., et al. 1995, *Sol. Phys.*, 162, 189
 Wilhelm, K., et al. 1997, *Sol. Phys.*, 170, 75
 Zangrilli, L., Nicolosi, P., Poletto, G., Noci, G., Romoli, M., & Kohl, J. L. 1999, *A&A*, 342, 592
 Zhang, T. X. 2003, *ApJ*, 597, L69